Topographical changes in photo-responsive liquid crystal films

Liu, Ling; Onck, Patrick R

Published in:
Soft Matter

DOI:
10.1039/c7sm02474f

Publication date:
2018

Soft Matter

PAPER

View Article Online
View Journal

Cite this: DOI: 10.1039/c7sm02474f

Topographical changes in photo-responsive liquid crystal films: a computational analysis†

Ling Liu and Patrick R. Onck*

Received 16th December 2017,
Accepted 13th February 2018

DOI: 10.1039/c7sm02474f

rsc.li/soft-matter-journal

Switchable materials in response to external stimuli serve as building blocks to construct microscale functionalized actuators and sensors. Azobenzene-modified liquid crystal (LC) polymeric networks, that combine liquid crystalline orientational order and elasticity, reversibly undergo conformational changes powered by light. We present a computational framework to describe photo-induced topographical transformations of azobenzene-modified LC glassy polymer coatings. A nonlinear light penetration model is combined with an opto-mechanical constitutive relation to simulate various ordered and corrugated topographical textures resulting from aligned or randomly distributed LC molecule orientations. Our results shed light on the fundamental physical mechanisms of light-triggered surface undulations and can be used as guidelines to optimize surface modulation and roughness in emerging fields that involve haptics interfacing, friction control and wetting manipulation.

1 Introduction

Responsive soft materials now attract attention for their potential as microscale actuators and functional components in integrated devices. Liquid crystal (LC) polymeric networks can undergo conformational transformations in response to diverse external stimuli.[1–6] Compared to thermal and electrical actuation which require embedded heating sources and electrodes, light stimulation is of interest due to the possibility of wireless application with precise spatio-temporal control, and the potential for miniaturization. Azobenzene is probably the most widely used chromophore which can be embedded into various polymeric systems to generate a photo-induced mechanical response.[7–10] Azobenzenes reach a maximal absorbance at wavelengths around 365 nm after which they undergo isomerization. Azobenzene-modified liquid crystal (Azo-LC) systems can respond to UV light when the chromophores are cross-linked to the polymer skeleton. As schematically shown in Fig. 1(a), the cross-linked azobenzenes isomerize from the natural rod-like *trans* state to the metastable bent-like *cis* state under the exposure of UV light. In contrast to the *trans* molecules which are aligned with the neighboring liquid crystal molecules, the *cis*-state azobenzenes decrease the orientational order of the network, leading to an anisotropic deformation. The Azo-LC network undergoes a contraction along the average direction of the molecules, which is denoted by the director $\vec{n}$ (see Fig. 1(a)), and an expansion in the plane perpendicular to the director. The reversion of the deformation occurs under heating or visible light illumination.

Different surface transformations can be designed given various boundary conditions and director distributions by utilizing the responsive deformation of Azo-LC systems. Experimental and theoretical research has been focused primarily on two typical kinds of shape changes: (i) bending, folding and origami/miuraori of freestanding films and (ii) surface texture changes of substrate-constrained coatings. If a LC polymer strip or plate is free of constraint, or just fixed at one end, bending behavior is expected when deformation gradients through the thickness can be created. Such deformation gradients can be realized by making use of light attenuation,[11–13] elastic property gradients,[12] or introducing nonuniform director patterns through the thickness.[14–17] Those large amplitude bending and curling deformations can be tailored to drive macroscopic locomotion of, *e.g.*, swimmers,[18,19] walkers,[5,20] motors[21] and artificial cilia.[22,23]

For thin coatings fixed to a stiff substrate, out-of-plane deformations are the only strains possible because the in-plane deformations are fully constrained. Since the photo-induced shape changes depend on the orientation of the director (see Fig. 1), the final surface transformation is a function of the director distribution in the plane of the coating. Based on this approach, Broer and co-workers established a series of liquid crystal glassy polymer coatings featuring light-driven topographical texture changes,[24–30] which can potentially be used for controllable mechanical friction[28,29] and wettability,[31–34] haptic feedback devices,[35] refreshable Braille displays,[36,37] cell motion control,[38] microfluidic manipulation,[32] drug delivery systems[1,39] and self-oscillating/self-cleaning surfaces.[30]

Micromechanics of Materials, Zernike Institute for Advanced Materials, 9747 AG, Groningen, The Netherlands. E-mail: p.r.onck@rug.nl

† Electronic supplementary information (ESI) available. See DOI: 10.1039/c7sm02474f

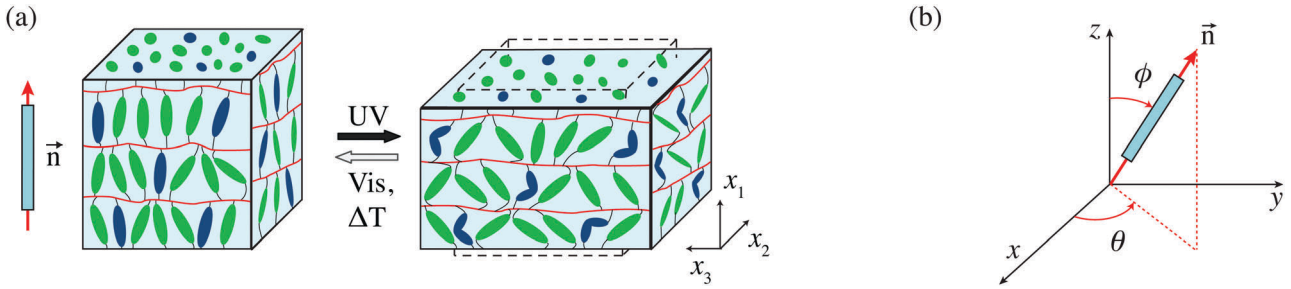

Fig. 1 (a) A schematic illustrating the mechanism of photo-triggered conformational changes of azobenzene-modified liquid crystal (Azo-LC) networks. The azobenzene molecules are in blue, the LC molecules in green and the polymer backbone in red. (b) Definition of the director orientation and its local reference frame (x_1, x_3 and x_3) in the global Cartesian coordinate system (x, y and z) by the tilt angle ϕ and the azimuthal angle θ. The arrows indicate the positive directions of the two angles, ϕ and θ, which range from 0 to 180 °C due to symmetry.

A full understanding of the underlying mechanisms and their translation into accurate theoretical and computational models are required to design and optimize these light-responsive topographies. Although there are a number of theoretical studies on the bending of freestanding structures with relatively simple director configurations,[40–44] the opto-mechanical response of light-triggered surface switching of substrate-constrained films with complex director distributions has still not been fundamentally explored. In this work, we present a computational framework that models the UV-triggered *trans*-to-*cis* isomerization process of the embedded azobenzene molecules and the resulting surface deformation of the Azo-LC films. The films studied here are schematically summarized in Fig. 2, featuring different texture transformations due to their distinct director distributions, *i.e.*, (a) linearly patterned films,[24,25,30] (b) polydomain films[29] and (c) fingerprint films.[27]

This article is organized as follows. In Section 2, the modeling framework is detailed that features two parts: (1) the opto-mechanical constitutive relation to describe photo-induced spontaneous deformations and internal stresses (2) the light attenuation equations that describe the director-dependent isomerization of azobenzenes. In Section 3, the results are presented for films with three types of director distributions. The predicted topographies are quantified by means of roughness parameters and the ensuing correlations to the experiments are explored. A detailed comparison is given in Section 4 between the different types of films and their dependence on the key system parameters, followed by the conclusion.

2 Computational model

2.1 Opto-mechanical constitutive equations

The constitutive relations are detailed here that describe the topographical changes resulting from the director-guided azobenzene isomerization described in Section 2.2.

The equilibrium and the kinematic equations follow as

$$\sigma_{ij,j} = 0, \tag{1}$$

and

$$\varepsilon_{ij} = \frac{1}{2}\left(u_{i,j} + u_{j,i}\right), \tag{2}$$

respectively, in which $()_{,j}$ denotes differentiation with respect to coordinate j, *i.e.*, $\partial()/\partial x_j$.

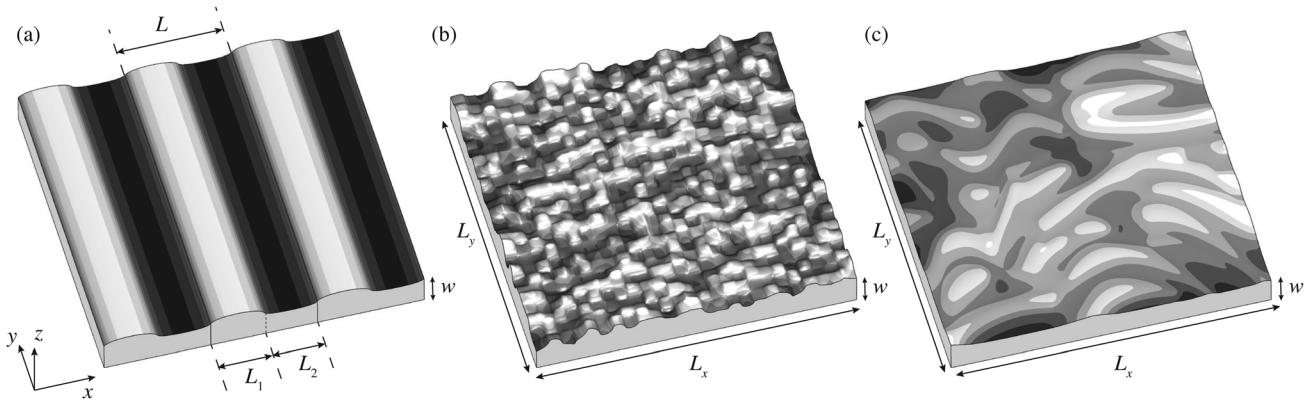

Fig. 2 Schematics summarizing the three Azo-LC films studied: (a) linearly-patterned films, (b) polydomain films and (c) fingerprint films. The linearly-patterned film is alternately made of two distinct director alignments. The polydomain film consists of multiple rectangular domains having directors that are randomly distributed. The fingerprint film features planar chiral nematic director distributions that are uniform through the thickness. The incoming UV light is exposed from the top (normal to the surface) and propagates in the negative z direction from $z = w$ towards the substrate at $z = 0$.

The components of the total strain tensor with respect to the local reference frame can be written as

$$\varepsilon_{ij} = \varepsilon_{ij}^{e} + \varepsilon_{ij}^{ph}, \quad (3)$$

where ε_{ij}^{e} and ε_{ij}^{ph} are the elastic and photo-induced strains, respectively. The subscripts i and j, run from 1 to 3, denoting the indices of the local coordinate system, as defined in Fig. 1(b). The local x_1-axis is along the director $\vec{n}$ so that the local x_2 and x_3 axes describe the plane perpendicular to the director.

The anisotropic photo-induced eigenstrains ε_{ij}^{ph}, are taken to be linearly proportional to the fraction of the *cis* molecules,[12,29,45] in line with a molecular dynamics study,[46]

$$\varepsilon_{ij}^{ph} = P_{ij} n_c, \quad (4)$$

where P_{ij} is the photo-responsivity tensor and n_c is the volume fraction of *cis* azobenzenes, see Section 2.2. The non-zero components of P_{ij} with respect to the local coordinate system are P_{11} and $P_{22} = P_{33}$, corresponding to the light-induced contraction and expansions along and perpendicular to the director, respectively. The photo-Poisson ratio $\mu^{ph} = -P_{22}/P_{11}$, is reported to range from 0.4 to 0.7 for different LC systems.[15,29,42] Here we take $\mu^{ph} = 0.6$, which results in a positive photo-induced volumetric strain $\varepsilon_{vol}^{ph} = (P_{11} + 2P_{22})n_c = (1 - 2\mu^{ph})P_{11}n_c = -0.2P_{11}n_c$ and indicates there is a volume increase (since $P_{11} < 0$) after the *trans*-to-*cis* isomerization process. This corresponds to an immediate density decrease, which was demonstrated through a density measurement for a free-standing liquid crystal film similar to the material tested here.[24] The magnitude of the photo-induced deformation of a Azo-LC system depends on the material composition, such as the concentration of the azobenzenes and their positions in the polymer skeleton,[47,48] the density and length of crosslinkers,[12,49–51] the initial order parameter before illumination[52] and is also related to the working temperature relative to the glass transition temperature of the system.[53] Here, we assume that all theses dependence are captured by the components P_{ij} and remain constant during the UV exposure.

We assume a linearly-elastic stress–strain relation,

$$\sigma_{ij} = C_{ijkl}\varepsilon_{kl}^{e} = C_{ijkl}(\varepsilon_{kl} - \varepsilon_{kl}^{ph}), \quad (5)$$

where C_{ijkl} are the components of the elastic stiffness tensor, and the Einstein summation convention is used for repeated indices. The liquid crystal polymer is considered to be a transversely isotropic material with rotational symmetry along the director and thus there are five independent mechanical constants, *i.e.*, the Young's modulus along the director E_{11}, the moduli perpendicular to the director $E_{22} = E_{33}$, the Poisson's ratios $\mu_{12} = \mu_{13}$ corresponding to a contraction perpendicular to $\vec{n}$ when an extension is applied along the director, the Poisson's ratio inside the isotropic plane μ_{23} and the shear moduli parallel to the director $G_{12} = G_{13}$. Recently, the Young's moduli of an Azo-LC film were found to decrease under illumination with strong intensities.[53] In the current work, the tested coatings are exposed to intermediate levels of intensity and thus we ignore the softening effect and the mechanical properties are kept constant during deformation. In addition, following a recent experimental study,[25] in which the contribution to the total strain of a temperature increase resulting from the absorption of the UV light was analyzed, we assume the photo-induced eigenstrains to be dominant and ignore the thermal effect in the constitutive relations, eqn (3) and (5). However, a fully coupled thermal-opto-mechanical simulation can readily be developed using the framework proposed here.

There are two different boundary conditions in this work, given the three different coatings with specific director distributions (Fig. 2). Periodic boundary conditions are used if a unit cell can be identified, such as the linearly-patterned films (see Fig. 2(a) and Section 3.4). For all the lateral surfaces, periodic boundary conditions are prescribed, so that each pair of opposite surfaces share the same displacements. All displacements at the bottom surface ($z = 0$) are fixed, while the top surface ($z = w$) is traction free. For the structures for which a unit cell cannot be identified, such as coatings with random director distributions (see Fig. 2(b) and (c) and Sections 3.5 and 3.6), a full size model will be built. Therefore, only the displacements of the bottom surface are confined and all the other surfaces are traction free. Large samples need to be constructed to properly pick up bulk behavior since edge effects are expected to develop near the free edges for this scenario.

Due to the anisotropy of the light-induced strains and the non-uniform distribution of n_c and the director, the spontaneous deformations will differ from region to region. The mismatch of theses deformations and the constraints imposed by the rigid substrate result in the development of mismatch stresses, which results in additional volume changes, since the elastic Poisson's ratio is less than 0.5 (typically 0.3).[29,54] Thus the interactions between different domains reshape the topography and should be accounted for in the description and the design of effective switchable textures.

2.2 Light attenuation model

The driving mechanism of the photo-responsive deformation of azo-modified liquid crystal polymers under UV exposure is the conversion of the azobenzenes from the *trans*-state to the *cis*-state (see eqn (4)). This *trans*-to-*cis* conversion depends on the wavelength and intensity of the incoming light, and the attenuation process through the thickness which critically depends on the director distribution. To account for this, the nonlinear light absorption model developed by Corbett and Warner,[40,45,55] is adopted and extended here to account for the director-dependent azobenzene isomerization evolution. At the beginning of the light attenuation process, all azobenzene molecules are in the natural *trans*-state, which leads to the exponential intensity profile following the Beer–Lambert law:[56] the attenuation is proportional to the intensity itself, $\partial I/\partial z = I(z)/d$, and thus $I(z) = I_0 e^{-z/d}$, where I_0 is the incident intensity and d is the attenuation length. This initial exponential profile will change in time, however, when the *trans*-state azobenzenes absorb the UV light and successfully isomerize to the *cis*-state, which has a much lower absorbance at the wavelength of the UV light than that of *trans*-state. As a result, the incoming light is considerably less absorbed due to the low absorbance of the *cis*

azobenzenes at the top surface, which makes the light penetrate deeper than predicted by the exponential Beer–Lambert law. This evolution of the light penetration can explain the mechanical response for heavily azo-dosed systems.[11] This non-linear light absorption model[40,45,55] is extended here with a polarization coefficient to account for the spatially-varying azobenzene conversion for nonuniform director configurations.

As shown in Fig. 2, we assume the incoming light to propagate along the negative direction of the z-axis, from the top surface $z = w$ to the bottom $z = 0$, where w is the thickness of the film. The dynamics of the azobenzene isomerization consists of three parts: (i) the light-induced *trans*-to-*cis* forward reaction, (ii) the light-induced *cis*-to-*trans* backward reaction, and (iii) the thermally-stimulated spontaneous *cis*-to-*trans* backward reaction. The intensity of the Poynting flux at location z and time t is denoted by $I(z,t)$. The volume fractions of the *trans* and *cis* molecules are denoted by n_t and $n_c = 1 - n_t$, respectively. The governing equations for the light penetration can be written as:[29,57]

$$\tau\frac{\partial n_t}{\partial t} = (1 + \beta\zeta\mathscr{I}(z,t)) - [1 + (\alpha + \beta)\zeta\mathscr{I}(z,t)]n_t(z,t), \quad (6)$$

$$\frac{\partial\mathscr{I}}{\partial z} = \left[\left(\frac{1}{d_t} - \frac{1}{d_c}\right)n_t(z,t) + \frac{1}{d_c}\right]\zeta\mathscr{I}(z,t), \quad (7)$$

where $\mathscr{I}(z,t) = I(z,t)/I_0$ is the reduced local light intensity and the parameters d_t and d_c are the attenuation lengths for the *trans* and *cis* azobenzene, respectively. The dimensionless coefficient α describes the capacity of the light to trigger the forward *trans*-to-*cis* transition with respect to the thermally-driven back-reaction. The β has a similar meaning but for the ability of the light to prompt the optically-triggered *cis*-to-*trans* back-reaction. The α and β scale with the input intensity and can be temperature-dependent since the thermal back-reaction is accelerated at high temperatures[45] and τ is the average lifetime of *cis* that depends on the ambient temperature.

The parameter ζ is the polarization coefficient and is defined for diffuse light illumination as[55]

$$\zeta = \frac{1}{3}\left[1 - SP_2(\cos\bar{\phi})\right], \quad (8)$$

where $\bar{\phi}$ is the angle between the director $\vec{n}$ and the propagating direction $\vec{k}$ (the negative z direction) and $P_2(x)$ is the second Legendre polynomial with $P_2(x) = (3x^2 - 1)/2$. Note that, from Fig. 1(b), it follows that $\bar{\phi} + \phi = \pi$. The order parameter S (scalar) describes the orientational order of the liquid crystal molecules with respect to the director $\vec{n}$, $S = \langle 3\cos^2\psi - 1\rangle/2$. The ψ is the angle between the LC molecules and the director and the average sign $\langle\cdots\rangle$ is taken over all molecules. We neglect the effect of order decrease during the photo-induced response here since the loss of the order in glassy Azo-LC polymers is usually small.[1,29]

The attenuation lengths d_t and d_c are related to the ratio of the quantum efficiencies $\eta = \eta_t/\eta_c$ by

$$\frac{d_t}{d_c} = \frac{\beta}{\alpha}\eta, \quad (9)$$

where η_t and η_c are the quantum efficiencies of the conversion from *trans* to *cis* and from *cis* to *trans*, respectively.[57,58]

One can get the evolution of the two azobenzene states after solving the coupled partial differential eqn (6) and (7) subject to the boundary conditions at the top surface $\mathscr{I}(w,t) = 1$ and the initial condition $n_t(z,0) = 1$. Here only the photo-stationary state is of interest for which the rate of the forward-reaction equals the sum of the two back-reactions, leading to a dynamic equilibrium state, $\partial n_t/\partial t = 0$. We can solve n_t and n_c as functions of $\mathscr{I}$ by substituting this in eqn (6), and obtain

$$n_t(z) = \frac{1 + \beta\zeta\mathscr{I}(z)}{1 + (\alpha + \beta)\zeta\mathscr{I}(z)}, \quad (10)$$

$$n_c(z) = \frac{\alpha\zeta\mathscr{I}(z)}{1 + (\alpha + \beta)\zeta\mathscr{I}(z)}. \quad (11)$$

If one substitutes eqn (10) into eqn (7), the resulting ordinary differential equation can be solved to yield the non-linear implicit relation[57]

$$\ln\mathscr{I} + \frac{(\alpha - \beta\eta)}{\beta(1 + \eta)}\ln\left(\frac{1 + \beta(1 + \eta)\zeta\mathscr{I}}{1 + \beta(1 + \eta)\zeta}\right) = \frac{\zeta}{d_t}(z - w). \quad (12)$$

The last equation can be solved for $\mathscr{I}(z)$ and the solution reduces to the Beer–Lambert law in the absence of isomerization (*e.g.*, under a weak light exposure, $\alpha \approx 0$ and $\beta \approx 0$).

3 Numerical results

The boundary value problems described in Section 2 are solved using the finite element method for which the commercially available package Abaqus/Standard is used.[59] 3D brick elements with reduced integration C3D8R are used in all simulations. The results of films containing uniform directors throughout are first presented to highlight the role of the mismatch stress in the difference between the pure photo-induced spontaneous response and the final volume changes (Section 3.3). Next, as schematically summarized by Fig. 2, the topographical changes of non-uniform coatings are further addressed, *i.e.*, the linearly-patterned films (Section 3.4), followed by coatings with more complex director configurations, *i.e.*, the polydomain (Section 3.5) and fingerprint films (Section 3.6).

3.1 Input parameters

All the default input parameters are discussed here and listed in Table 1. The attenuation length of the *trans* azobenzene d_t depends on the wavelength of the input light and the concentration of the azobenzenes. The dimensionless light parameters α and β depend on the intensity and wavelength of the light source. The values of these parameters can be determined by fitting the results of the light attenuation model to the transmittance measurement as done in our previous study.[29] Here, $w/d_t = 10$, $\alpha = 30$ and $\beta = 3$ are taken, unless specified otherwise. The quantum efficiency ratio is chosen to be equal to a previously-reported value $\eta = 3$ (see ref. 45 and 54). The order parameter S is set to be 0.6, a typical value for glassy LC networks.[60] For the elastic properties of the liquid crystal polymers, the two

Table 1 A summary of the default input parameters

Light parameters		Elastic properties		Photo-responsivity properties	
α	30	E_{11} (MPa)	1000	P_{11}	−0.2
β	3	$E_{22} = E_{33}$ (MPa)	500	P_{22}	0.12
η	3	$\mu_{12} = \mu_{13}$	0.3	$\mu^{ph} = -P_{22}/P_{11}$	0.6
d_t/w	0.1	μ_{23}	0.3		
S	0.6	G_{12} (MPa)	384.6		

Young's moduli are selected close to the measured values:[29] E_{11} = 1 GPa and $E_{22} = E_{33}$ = 0.5 GPa. We set $\mu_{12} = \mu_{13} = \mu_{23}$ = 0.3, which is a typical value for the mechanical Poisson's ratio of glassy LC polymers,[15,54] in contrast to the incompressibility of rubber-like LC elastomers (μ = 0.5).[61] The shear modulus along the director is selected as $G_{12} = G_{13} = E_{11}/2(1 + \mu_{12})$ = 384.6 MPa. For the opto-mechanical properties, we follow our previous work[29] to set P_{11} = −0.2 and $P_{22} = P_{33}$ = 0.12 and thus the photo Poisson ratio $\mu^{ph} = -P_{22}/P_{11}$ = 0.6, as mentioned before.

3.2 Light profiles

Results are first presented for the director-dependent light penetration and azobenzene isomerization. We assume a coating with uniform director and diffuse light is exposed normally to the surface. In this case the only influencing variable is the tilt angle ϕ which comes in through the polarization coefficient ζ (eqn (8)). Under diffuse light illumination, the cholesteric phase,[24,25] where the director gradually changes the orientation along a pitch axis perpendicular to the substrate (see Fig. 5(a) and (b), *vide infra*), has the identical isomerization and light profile relative to the uniform planar director. For more complex situations, such as under polarized light exposure,[11,13,30] the azimuthal angle θ also plays a role. Nonuniform tilt angle configurations through the thickness, such as in the splayed configuration,[62,63] are not studied here.

The volume fraction of the *cis*-state azobenzene averaged through the thickness of the film, $\overline{n_c} = \frac{1}{w}\int_0^w n_c \mathrm{d}z$, is shown as a function of the tilt angle ϕ and the film thickness normalized by the attenuation length of the *trans* azobenzene w/d_t in Fig. 3(a) (see Fig. S1, ESI† for the dependence of n_c and $\mathscr{I}$ on z for α = 30 and β = 3). For illustration purpose, results for an intermediate light intensity $\alpha = 10\beta$ = 30 and a low intensity $\alpha = 10\beta$ = 5 are presented. For small thicknesses, *e.g.*, $w/d_t \leq 10$, the overall *cis* conversion level is the highest when $\phi = 90^\circ$, *i.e.*, the director $\vec{n}$ is perpendicular to the propagating direction of the incoming light $\vec{k}$, leading to the highest polarization coefficient ζ. When $\phi = 0^\circ$, *i.e.*, the director is parallel to the propagating direction of the light and perpendicular to the electric fields of the light, there is still *cis* conversion due to a fact that the order parameter of the system $S < 1$ and some off-axis azobenzenes are still capable of absorbing the incoming light, leading to considerable isomerization. However, this trend is reversed for larger values of w/d_t, *e.g.*, $w/d_t \geq 15$, and more significantly in the results with larger intensity (α = 30) than the low intensity. More insight can be obtained by observing the n_c and reduced light intensity through the thickness (see Fig. S1(a) and (b) in ESI†). The light is maximally attenuated for the planar director case ($\phi = 90^\circ$), which leads to a significant decrease of n_c for a deeper propagating depth because the weaker light intensity produces less successful *cis* conversion. The light attenuation for the homeotropic case ($\phi = 0^\circ$) is lower, resulting in a more uniform distribution of the *cis* azobenzene through the thickness and thus a larger overall conversion if a large thickness is taken.

In Fig. 3(b), the variation of $\overline{n_c}$ is shown against ϕ and $\alpha = 10\beta$ with w/d_t = 10. As the input light intensity increases, the overall *cis* conversion is enhanced for all situations, and reaches a plateau, which convergences to $\alpha/(\alpha + \beta)$ as $\alpha \to \infty$ (see eqn (11)). The *cis* conversion is more uniform through the film thickness as α increases (see Fig. S2, ESI†).

3.3 Uniform films

In this section we analyze the deformation of Azo-LC films in which the directors are uniform throughout. A coating infinitely large in the x–y plane is considered to avoid edge effects, by periodic boundary conditions on all lateral surfaces, with the bottom surface fixed and the top surface traction free. Due to the

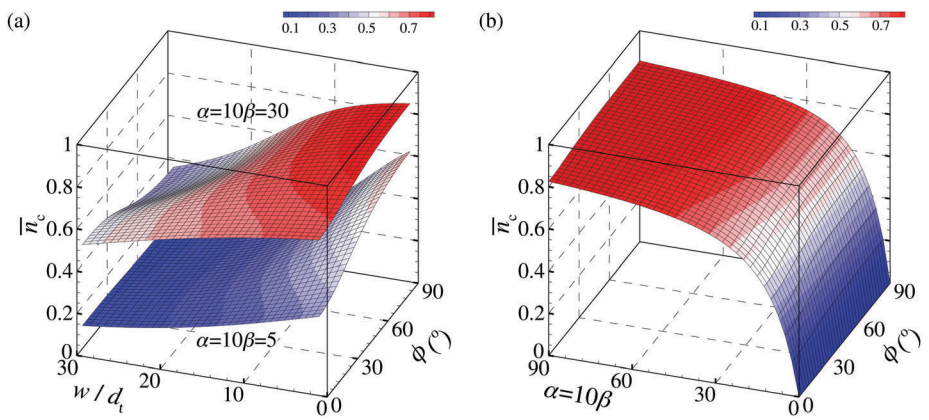

Fig. 3 The overall *trans*-to-*cis* conversion averaged through the thickness, $\overline{n_c}$, inside a film as a function of (a) the tilt angle ϕ and the thickness normalized by the attenuation length of the *trans* azobenzene w/d_t with $\alpha = 10\beta$ = 30 and 5; and (b) as a function of ϕ and $\alpha = 10\beta$ with the thickness being w/d_t = 10.

rotational symmetry along the z-axis, the final surface height change only depends on the tilt angle, ϕ. The pure photo-induced spontaneous volumetric change averaged through the thickness ε_{vol}^{ph} and the total volumetric change consisting of both photo-induced and stress-induced contributions, ε_{vol}, are obtained from

$$\varepsilon_{vol}^{ph} = \frac{1}{w}\int_0^w \varepsilon_{ii}^{ph} dz, \quad \varepsilon_{vol} = \frac{1}{w}\int_0^w \varepsilon_{ii} dz,$$

respectively. Due to the periodic boundary condition, which leads to $\varepsilon_{xx} = 0$ and $\varepsilon_{yy} = 0$, it results in that $\varepsilon_{vol} = \int_0^w \varepsilon_{zz} dz/w$.

Comparison between ε_{vol}^{ph} and ε_{vol} is shown in Fig. 4 as a function of the tilt angle for three different photo-Poisson ratios, $\mu^{ph} = -P_{22}/P_{11} = -P_{33}/P_{11} = 0.2$, 0.6 and 1 and for three coating thicknesses, $w/d_t = 5$, 10 and 20. The simulations are conducted by fixing $P_{11} = -0.2$ and changing P_{22} and P_{33}, so that $\varepsilon_{vol}^{ph} = (1 - 2\mu^{ph})P_{11}n_c = -0.2(1 - 2\mu^{ph})n_c$. If $\mu^{ph} < 0.5$, the photo-induced *trans*-to-*cis* isomerization gives rise to a spontaneous volume decrease, $\varepsilon_{vol}^{ph} < 0$. The opposite ensues for the cases with $\mu^{ph} > 0.5$ and the effect is enhanced with increasing μ^{ph}.

The total volume change (that includes the elastic strain) resulting from the substrate constraint depends on the tilt angle as well on μ^{ph}. For the homeotropic director alignment ($\phi = 0^\circ$), compressive stresses are generated due to the photo-induced expansions inside the x–y plane and thus the volume is decreased due to the fact that $\mu < 0.5$. This mechanically-induced volume decrease effect is larger for higher μ^{ph} since larger compressive stresses occur for larger expansions perpendicular to the director.

On the other hand, for the planar director ($\phi = 90^\circ$), the photo-triggered contraction along the director induces tensile stresses and the spontaneous expansion perpendicular to the director induces compressive stresses, leading to a final volume change which is determined by the competition between the tensile and compressive stresses. For smaller photo-Poisson ratios, *e.g.*, $\mu^{ph} = 0.2$ and 0.6 in Fig. 4, the tensile stress is dominant and the final volume is increased upon the original photo-triggered volume change. For the case $\mu^{ph} = 1$, the effect from the tensile and compressive stresses almost cancel out, resulting in a small volume change in addition to the spontaneous response.

From the dependence of the photo-triggered volume change against the tilt angle, it is of interest to note that ε_{vol}^{ph} is the highest for the planar director scenario for $w/d_t = 5$ and 10, but the trend is reversed for $w/d_t = 20$. This is attributed to the fact that the bulk *cis* concentration determines the volume change (see eqn (4)) and the thickness-averaged *trans*-to-*cis* conversion for the planar director is lower than that of the homeotropic case for coatings with large thicknesses (see Fig. 3(a) and Fig. S1(a), ESI†), even though the n_c is largest near the top surface for the former case. Furthermore, the results of the final volume change for the planar director are the same as those of the cholesteric phase since their *cis* conversion levels are identical.

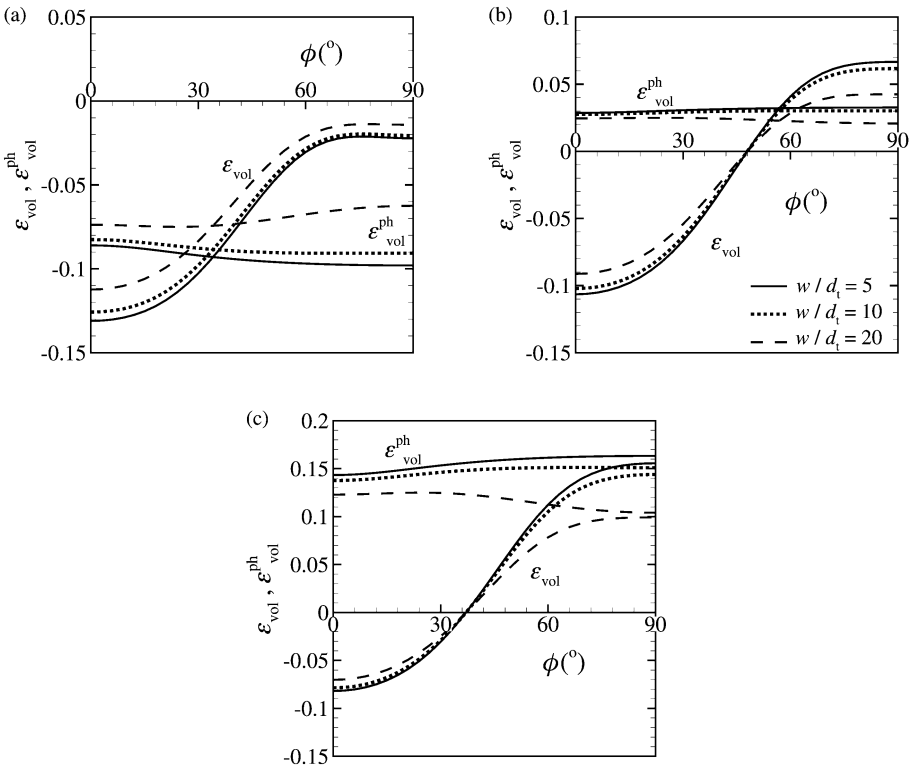

Fig. 4 Variation of the photo-induced volumetric change ε_{vol}^{ph} and the total volumetric change ε_{vol} averaged through the thickness against the director tilt angle ϕ with three different thicknesses, $w/d_t = 5$, 10 and 20, for uniform director films with various photo-Poisson ratios: (a) $\mu^{ph} = 0.2$, (b) 0.6 and (c) 1.

3.4 Linearly-patterned films

The first type of Azo-LC coating tested here with nonuniform director distribution is the linearly patterned film. Taking advantage of the anisotropic deformation ($P_{11} < 0$ and $P_{22} = P_{33} > 0$), we study a coating with an alternating cholesteric/homeotropic director alignment under flood light illuminated,[25] see Fig. 5(a). For comparison, we also analyze a cholesteric coating with uniform director under localized illumination, see Fig. 5(b), leading to a corrugated surface change between the exposed and unexposed regions.[24] The homeotropic phase has a director that is perpendicular to the substrate and the cholesteric phase (a.k.a. the chiral nematic phase) features a continuous director rotation through the thickness, with a pitch length L_{pt}, denoting the distance over which the director makes a full 360° rotation. The patterning direction is along the x-axis and the coatings are uniform along the y-axis (see Fig. 2(a)). In the experiments, some minor surface reliefs might be present after fabrication (but before illumination), due to the Marangoni effect during the photo-polymerization step. We ignore this effect for all the simulations in this work and assume all the original top surfaces to be perfectly flat.

As schematically shown in Fig. 5(a) and (b), unit cells with dimensions $L \times w$ (along the x and z axis, respectively) are constructed, in which the bottom surfaces are perfectly bonded to the substrate, periodic boundary conditions are used at all the lateral surfaces and the top surfaces are traction free. Here we have 5 characteristic length scales: L_1, L_2, w, d_t and L_{pt}. We take the default thickness $w/d_t = 10$ and study the effect of the other two dimensionless numbers: L/w and L_1/L_2, where $L = L_1 + L_2$ is

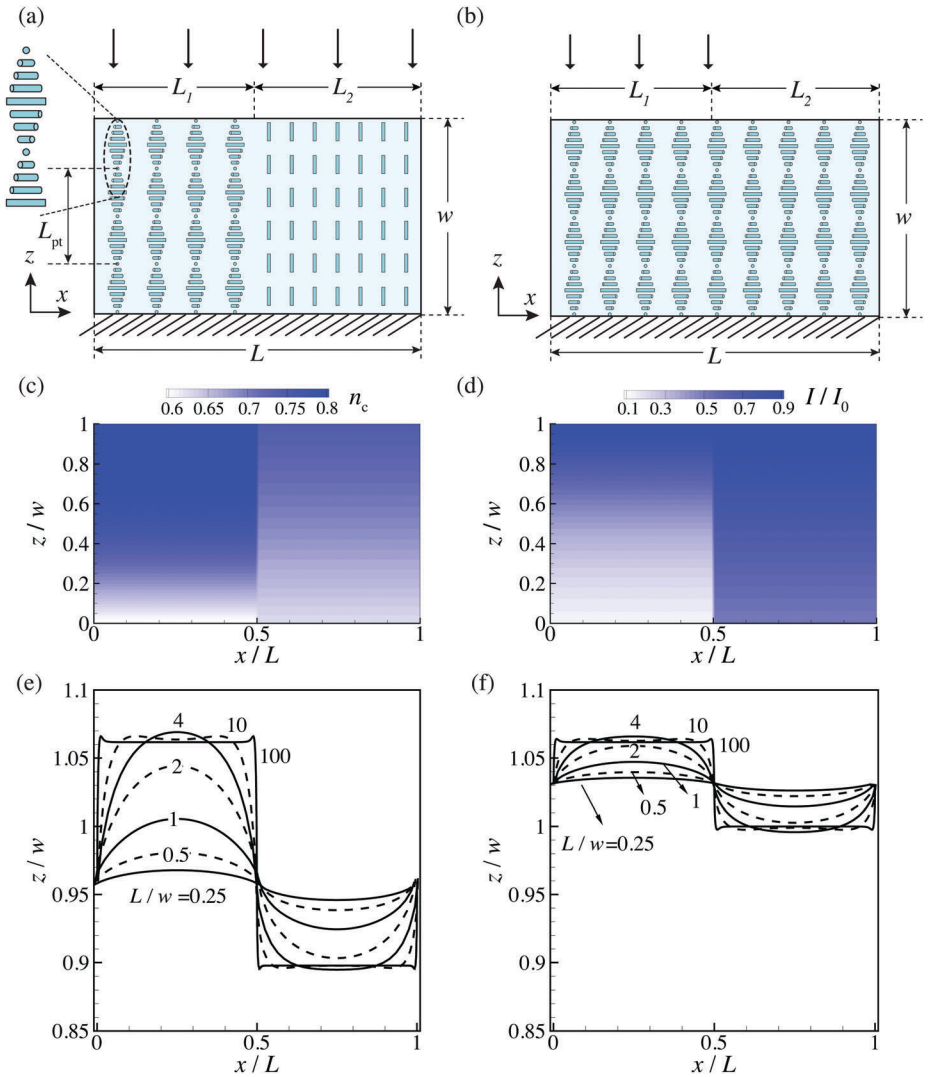

Fig. 5 Effect of the in-plane size on the topographical changes of linearly-patterned films. (a and b) Schematics depicting the unit cells of two patterned films: the cholesteric/homeotropic film under flood exposure and the uniform cholesteric film under localized illumination, where w is the thickness, L_i denotes the length along the x axis for the two phases (i = 1 and 2) and L is the length of the unit cell, $L = L_1 + L_2$. (c and d) Contour plots of *cis* conversion n_c (c) and reduced light intensity I/I_0 (d) inside the cholesteric/homeotropic film under illumination with $\alpha = 10\beta = 30$ and $w/d_t = 10$. (e and f) Normalized surface profiles of the two patterned films ((e): cholesteric/homeotropic; (f): uniform cholesteric) with increasing L/w and $L_1 = L_2$. Note that only two pitches are drawn in the cholesteric phase in (a and b) for clarity but $w/L_{pt} = 4$ is used in all the simulations.

the length for the whole unit cell, and the sizes for each domain are L_1 and L_2. Here we assume four full pitches along the thickness, $w/L_{pt} = 4$, and the director at the bottom is oriented along the y-axis, $\theta|_{z=0} = 90^\circ$ (see Fig. 5(a) and (b)). It is found that if the number of the pitches through the thickness is large enough ($w/L_{pt} \geq 4$), the resulting surface topographies are independent of the pitch number and the director alignment at the bottom.[64] For a detailed discussion related to the influence of w/L_{pt} and the starting angle of the pitch, please see our previous work.[64]

The photo-stationary *trans*-to-*cis* conversion and the light attenuation are shown in the contour plots of Fig. 5(c) and (d), respectively, for the cholesteric/homeotropic film. The director-dependent isomerization and light penetration are clearly shown. The n_c is the highest on the top surface of the cholesteric phase and decreases dramatically due to the heavier light attenuation (Fig. 5(d)). Meanwhile the *cis* conversion in the homeotropic phase is more uniform, attributed to the lower light absorption.

3.4.1 Effect of the in-plane sizes. Topographical changes of the two types of films are shown in Fig. 5(e) and (f), respectively, in which the heights are normalized by the thickness w and the horizontal axes are normalized by unit cell length L. The simulations are conducted by fixing the thickness w and increasing the unit cell length L, with $L_1 = L_2$. For the cholesteric/homeotropic patterned coating depicted in Fig. 5(a), the mechanical interaction between the two domains is intense for small in-plane sizes, *i.e.*, $L/w < 1$, and the out-of-plane light-driven expansion of the cholesteric phase is almost fully suppressed by the adjacent homeotropic regions that are contracting (Fig. 5(e)), leading to an overall contraction of the film ($z/w < 1$). This is attributed to the fact that the magnitude of the expansion of the cholesteric phase, which is perpendicular to its director, is smaller than the contraction along the director of the homeotropic phase combined with the Young's modulus is higher for the homeotropic part along the thickness direction since it is parallel to the orientation of the director. The cholesteric part continues to expand (and the homeotropic to contract) relative to the original surface height ($z/w = 1$) as L/w increases, until the surface profile converges to a shape with a pair of rectangular protrusions and trenches for very large L/w values.

For the film with a uniform cholesteric phase under localized illumination, the illuminated area expands and lifts the unexposed region up to the level where the height over thickness ratio is larger than 1 for small L/w (see Fig. 5(f)). This effect gradually decreases with increasing L/w, for which the height of the exposed region converges to the height of the cholesteric phase in the alternating patterned film in Fig. 5(e), while the un-exposed region finally falls back to the original height, indicating a diminishing of the mechanical interaction between the exposed and unexposed areas.

More detail of the stress development and its effect on the topography is shown in Fig. 6 for the cholesteric/homeotropic film with $L/w = 1$, 2, 4 and 20. The in-plane stresses σ_{xx} feature a cyclic pattern following the director rotation along the pitch through the thickness. For small L/w the out-of-plane stress σ_{zz} inside the cholesteric phase is compressive and it is tensile inside the homeotropic part. The σ_{zz} is large in coatings with small in-plane sizes ($L/w \leq 4$), which is indicative of the mechanical constraint that suppresses the expansion in the cholesteric part and the contraction in the homeotropic part. The out-of-plane stress σ_{zz} gradually diminishes in each domain away from the domain interfaces as L/w increases, leading to the maximal deformation of each region in the unconstrained limit, and the σ_{zz} only remains near the domain boundaries, as shown in the film with $L/w = 20$ in Fig. 6.

The experimental control of the patterned film sizes relies on current techniques of director alignment for the alternating patterns[25,28] and on lithographic processing of photo-masks which are used for local illumination.[24] By using electrical fields to construct a patterned director alignment before photo-polymerization, the geometries are limited by the gap size of the electrode array.[25] For the thickness and in-plane size selection in the experiment, typically $L/w \geq 50$,[24,25,28] for which the measured surface profiles attain rectangular shapes, in agreement with our predictions (see Fig. 5(e) and (f)). However, to explore the limits of the resolution of director alignment control at smaller length scales,[2,10,65–67] it is of interest to note that reducing L/w to small values will enhance the mechanical constraints and thus will reduce the out-of-plane feature sizes.

In order to quantitatively characterize the resulting surface topographies, we introduce three areal roughness parameters. Let us define the discretized point set of the top surface to be expressed by the points (i,j) with corresponding coordinates $(x(i,j),y(i,j),z_0)$ before actuation, where $i = 1, 2,\ldots M, j = 1, 2,\ldots N$, $z_0 = w$ is the original height and $N \times M$ is the number of points. During illumination each point undergoes the displacements $(u_x(i,j),u_y(i,j),u_z(i,j))$.

The Arithmetic Average Height,[68] S_a, is widely used to characterize rough surfaces in relation to their friction and wear properties.[69–71] It describes the average vertical displacement of the protrusions and trenches relative to the mean surface and is defined as

$$S_a = \frac{1}{MN}\sum_{i=1}^{M}\sum_{j=1}^{N}|\overline{u_z}(i,j)|, \tag{13}$$

where $\overline{u_z}(i,j) = u_z(i,j) - r_z$ and r_z is the mean surface height change, defined as

$$r_z = \frac{1}{MN}\sum_{i=1}^{M}\sum_{j=1}^{N}u_z(i,j).$$

The second areal roughness introduced here is the classical dimensionless Wenzel roughness,[72] in light of the possible application of the reversible topographies in wetting control, defined as

$$R = \frac{A_{real}}{A_{proj}}, \tag{14}$$

where A_{real} is the real surface area and $A_{proj} \leq A_{real}$ is the projected surface area onto the x–y plane. The third roughness

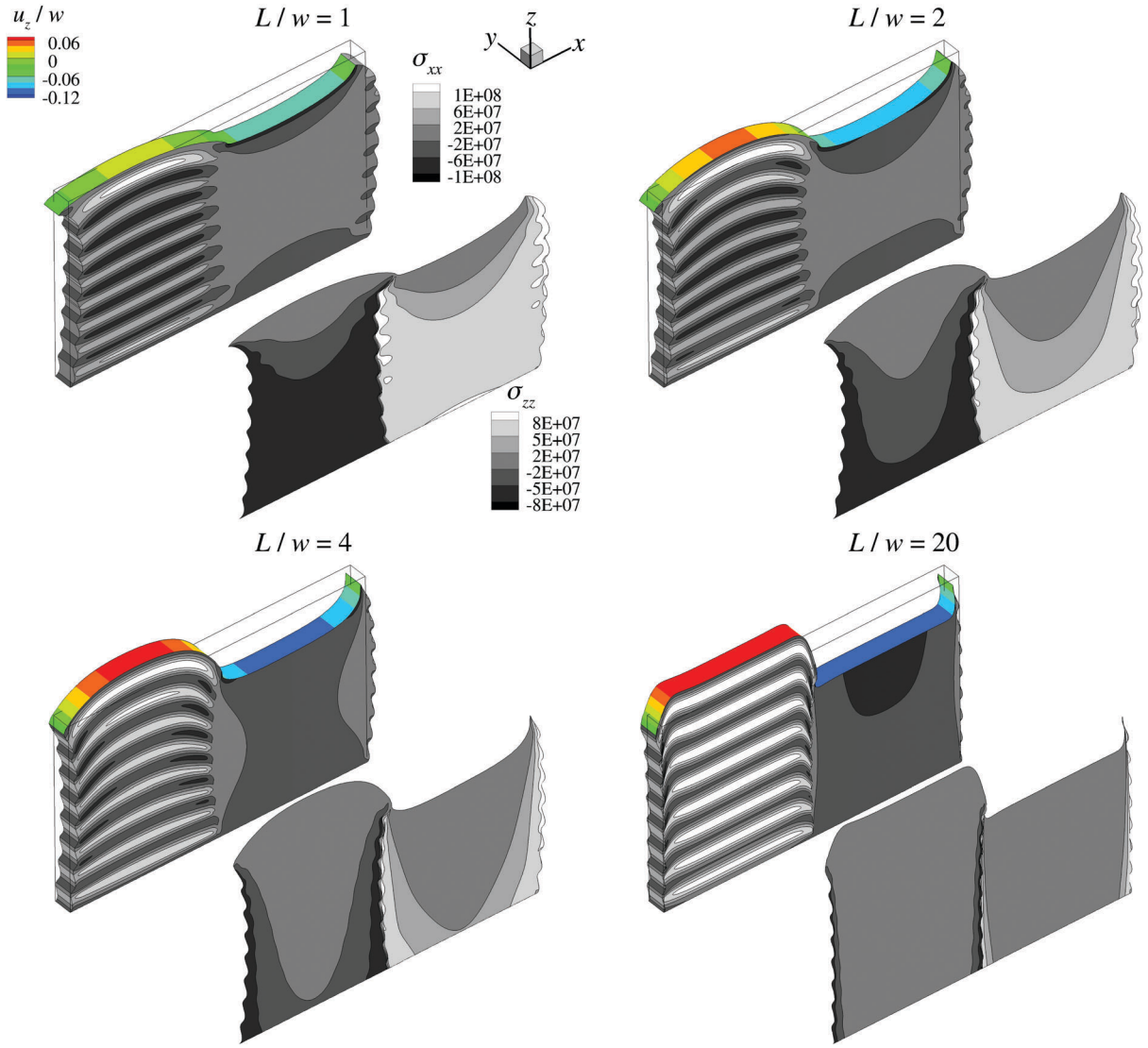

Fig. 6 Normalized 3D topographies of the cholesteric/homeotropic patterned film superimposed with contour plots showing the normalized out-of-plane displacement u_z/w at the top surface, the distribution of the in-plane stress component σ_{xx} on the lateral surfaces and the out-of-plane stress σ_{zz} on the shifted duplicate surface. Results are shown for four different unit cell lengths: L/w = 1, 2, 4 and 20.

parameter is the modulation depth,[27,73] defined as the vertical distance between the highest and the lowest point of the surface

$$\text{modulation} = \max_{(i,j)}(\overline{u_z}(i,j)) - \min_{(i,j)}(\overline{u_z}(i,j)). \quad (15)$$

The modulation depends only on the two maximally displaced points on the whole surface and lacks local information. For a simple sinusoidal-like surface texture (*e.g.*, the linearly-patterned films), the modulation nicely quantifies the surface topography, but for the randomly corrugated surfaces (*e.g.*, the polydomain and fingerprint films, *vide infra*), we only use S_a and R. Here we will focus on S_a and R and come back in Section 4 for a detailed roughness comparison including the modulation.

Fig. 7(a) plots the roughness parameters, *i.e.*, the average height normalized by the thickness S_a/w and the Wenzel roughness R, of the two films with flood and local illumination. The results of S_a/w and R for the cholesteric/homeotropic film are higher than those of the uniform cholesteric film under local exposure, due to the opposite and collaborative deformations in the two constituent domains for the former case. The normalized average height first increases with L/w and finally converges to 0.08 for the cholesteric/homeotropic film. For smaller in-plane sizes, the two domains are subjected to severe mechanical constraints (see Fig. 6), leading to a reduced S_a/w. The mechanical constraints are lower for larger L/w so that the two domains are more free to achieve their maximal out-of-plane deformations, as shown in Fig. 5(e) and (f). In contrast, the Wenzel roughness R is found to decrease with an increase of the in-plane dimension. Even though the absolute value of the surface change is lower for small in-plane sizes, the reduced dimensions lead to an increase of the Wenzel roughness. As $L/w \geq 20$, the Wenzel roughness converges to 1 when $L/w \to \infty$.

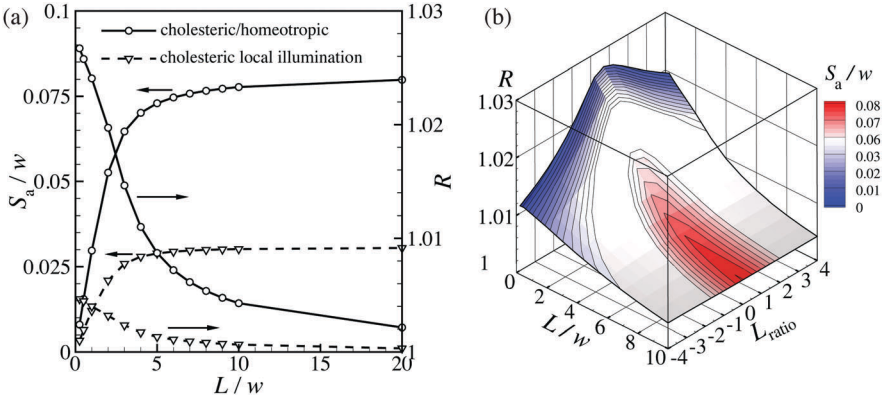

Fig. 7 (a) Variations of the average height normalized by the thickness S_a/w and the Wenzel roughness R of the two patterned films from Fig. 5 as functions of L/w. (b) Variations of the two roughness parameters for the cholesteric/homeotropic film with various L/w and different relative length configurations, characterized by L_{ratio}.

The remaining characteristic length scales are the lengths of the two constituent domains, L_1 and L_2. Here we define the relative length ratio as

$$L_{ratio} = \frac{L_1 - L_2}{\min(L_1, L_2)},$$

e.g., if $L_1 = iL_2 \geq L_2$, then $L_{ratio} = i - 1$ and if $L_2 = iL_1 \geq L_1$ then $L_{ratio} = 1 - i$. The dependence of R and S_a/w on L/w and the relative length ratio L_{ratio} for the cholesteric/homeotropic patterned film is shown in Fig. 7(b). It is found that a large roughness output R and S_a can be generated under $-1 \leq L_{ratio} \leq 1$ (*i.e.*, $0.5L_2 \leq L_1 \leq 2L_2$), for which both constituent phases are capable of contributing to the final surface change, while mechanical constraints severely reduces the roughness for length ratios outside that range.

3.4.2 Transition regions. Due to the self-assembling nature of liquid crystal molecules in the nematic monomer state, the alignment patterning (*e.g.*, in the cholesteric/homeotropic film) depends on applied external (electric) fields, surface anchoring conditions and the neighboring LC molecules. A transition region is expected to form between two domains with different alignments, in which the directors gradually rotate from one orientation to the other. After polymerization, the director configuration is frozen and the transition region stays.[24,25,30] The transition length was reported to be in the micrometer range for a coating with a thickness of 4 μm.[25] In the simulations performed above, the steps of the director at phase boundaries are assumed to be perfect: the directors are changing instantly from one orientation to the other. In the ESI,† we conduct a study on the effect of the transition region. The results are summarized as follows.

A planar/homeotropic patterned film incorporating transition regions is studied (see Fig. S3(a) in ESI†), in which the alignment of directors near the patterning boundaries gradually rotates from being parallel to the plane to being perpendicular to the plane, following a clockwise or counterclockwise scheme. It is found that transition regions featuring a counterclockwise director rotation induce the formation of peaks (see Fig. S3(b), ESI†). On the other hand, a valley is generated at the clockwise rotation region. This is due to the accumulation of out-of-plane shear strains of tilted director areas. These results qualitatively matches the experimentally-measured surface profile featuring a pair of peaks and valleys located at the domain boundaries or defect lines.[24,30] The counterclockwise transition region increases the roughness output (see Fig. S3(c), ESI†), while the clockwise region lowers the roughness. The effect is found to increase as the width of the transition region increases (Fig. S3(c)), see ESI† for more details on the study of transition regions.

3.5 Polydomain films

The next topographical switching morphology analyzed here is the polydomain film,[29] which features easy manufacturing, random domain-wise corrugated surfaces upon actuation and the possibility of downsizing the characteristic texture length. Fluorinated acrylates are added into the liquid crystal monomer mixtures before spin coating to construct polydomain films.[29] Due to the partial insolubility, the acrylates become obstacles and disturb the long-range orientational ordering, creating domains with short-range director alignment with controllable dimensions. Inside each domain, the director is uniform throughout, but the directors align differently from one domain to the other without any alignment preference. A certain variation in the in-plane domain size was found, owing to the fact that the undissolved droplets of the fluorinated molecules are not uniformly dispersed.[29] Generally controlled by the concentration of the fluorinated monomers, the domains have typical in-plane sizes in the range approximately from 5 μm to 30 μm with a thickness of 5 μm.

In our simulations, the polydomain films are discretized into square domains with equal sizes and the borders between the domains are assumed to be perpendicular to the substrate. The tilt angle ϕ and azimuthal angle θ of the directors (see Fig. 1(b)) in each domain are randomly picked from a uniform distribution in the range $[0,2\pi]$. Due to this random configuration, the light penetration and *trans*-to-*cis* conversion level differs from domain to domain as a function of the corresponding director tilt angles (see Fig. 3). Although the azimuth angle does not affect the light attenuation process, it does play a role in the

final topographical change due to the director-guided photo-responsive deformation of each domain. There are three characteristic length scales in the system: the in-plane size of a domain L, the thickness w and the attenuation length d_t from which we can define two dimensionless numbers: the aspect ratio L/w and w/d_t. Here we take the default thickness, $w/d_t = 10$ (Table 1), and analyze the polydomain films with increasing aspect ratio by fixing thickness w and varying L. The total lateral dimensions of the films, L_x and L_y (see Fig. 2(b)), are taken to be much larger than the domain size L and the thickness w, so that free edge effects due to the traction-free outer boundaries remain localized to the edges. The coating is perfectly bonded to the substrate and the top surfaces are traction-free.

The 3D surface transformations after UV exposure of one simulated polydomain sample film with aspect ratios $L/w = 0.5$, 1, 2 and 4 are shown in Fig. 8, with zoomed-in highlighted parts superimposed by contour plots for the normalized out-of-plane displacement u_z/w. The results are scaled to have the same in-plane size for easy comparison. 3D corrugated textures are obtained due to the random director distribution and the amplitude of the surface change strongly depends on the aspect ratio. To illustrate the evolution of the topographical shape with increasing L/w, normalized surface profiles extracted from a x–z cross-section (at $y = L_y/2$) are plotted in Fig. 9(a). An increase of the aspect ratio gives rise to a larger height change and makes the domains deform into step-wise textures. The normalized average height and Wenzel roughness based on four different random director distributions are shown in Fig. 9(b) as a function of L/w. The S_a/w keeps increasing with increasing aspect ratio until it reaches a limit value at around 0.055. The effect of the mechanical constraints resulting from the spontaneous deformation mismatch from the neighboring domains diminishes at larger aspect ratios, so that each domain is free to achieve large out-of-plane deformations, similar to the linearly-patterned coatings. The Wenzel roughness R also decreases with increasing aspect ratio, and converges 1 for larger in-plane domain sizes as also observed for the results given in Fig. 7(a). The simulations are also extended to consider nonuniform rectangular domain

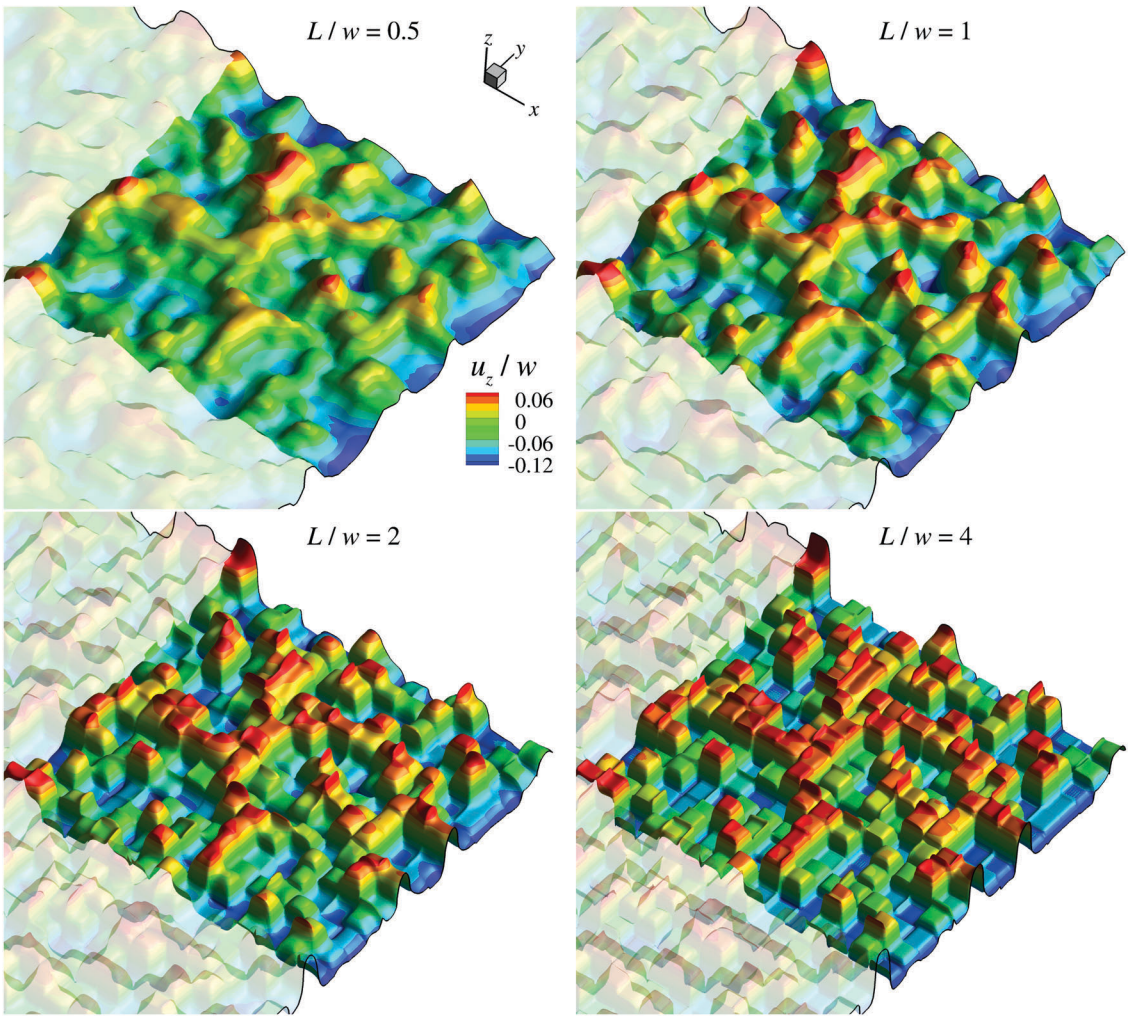

Fig. 8 Predicted 3D surface topographies of a polydomain film with square domains of size L superimposed with contour plots for the normalized displacement along the thickness direction u_z/w with aspect ratios $L/w = 0.5$, 1, 2 and 4. All the coatings are scaled to have the same size and only portions of the films are zoomed-in for a clear view.

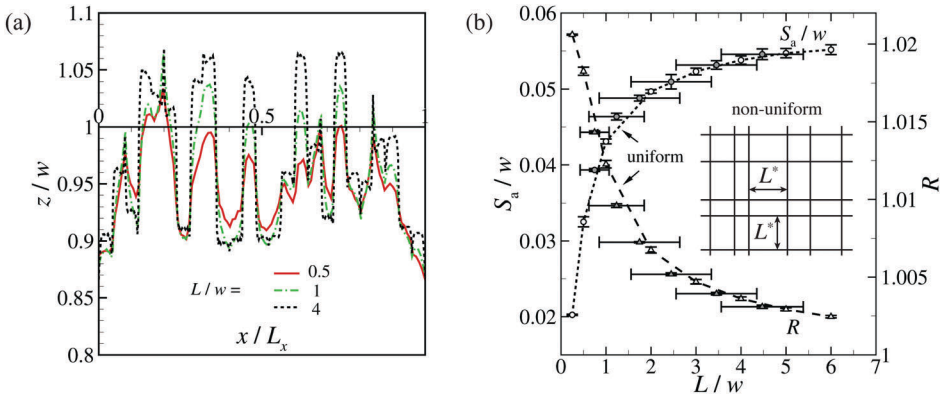

Fig. 9 (a) Comparison of the normalized surface profiles at a fixed x–z cross section from Fig. 8. (b) Variation of the normalized average height S_a/w and the Wenzel roughness R as functions of the aspect ratio. For the uniform square domain size the horizontal variable is equal to L/w, while for the random rectangular domains the horizontal variable is the average of the sizes L^*. The horizontal and the vertical error bars indicate the standard deviation of the domain size range and the roughness, respectively. The inset schematically shows a top view of the nonuniform polydomain film with size L^*.

sizes and shapes, which more closely resembles the real samples.[29] As schematically shown in the inset of Fig. 9(b), the domains are now assumed to be rectangles, whose side lengths can be varying throughout the film. The side lengths of the nonuniform domains, L^* in Fig. 9(b), are picked from a uniformly random distribution in a prescribed range, indicated by the horizontal error bars, and chosen such that the sum of all the individual domain lengths is equal to the total film dimensions, L_x and L_y. The predicted normalized averaged height and the Wenzel roughness are shown in for several nonuniform polydomain films, in which the vertical error bars are the standard deviations based on four nonuniform polydomain samples. The averaged values of the roughness parameters remain the same for the nonuniform and regular polydomain films. The scatter in the average height remains the same and that of the Wenzel roughness decreases.

3.6 Fingerprint films

The last type of films simulated in this work is the ''fingerprint'' coating,[27] which is made of planar cholesteric regions[27,74–78] with its helix axis being parallel to the substrate, in contrast to the cholesteric patterned films in Fig. 5, where the helix axis is perpendicular to the substrate. A regular fingerprint configuration can be created with extra effort in the surface treatment to force all the cholesteric pitches to be parallel to each other,[27,79] as schematically shown in Fig. 10(a) and 11(a). However, a unique random fingerprint film is usually obtained, featuring a complex pitch arrangement and thus serpentine textures are formed, just like human ''fingerprints'', (see Fig. 2(c) and 12).

As given in Fig. 10(a), we assume all the pitch helices to be parallel to the x-axis, with a uniform pitch length L_{pt} throughout the film. The director orientation is uniform through the thickness and the system is uniform along the y-axis. The near-homeotropic parts contract and regions with near-planar director expand, leading to surface undulations. We take one full pitch as a unit cell, with periodic boundary conditions applied upon all lateral surfaces (see the inset of Fig. 10(a)). The key characteristic dimensionless length of the regular fingerprint films is the ratio of the pitch length to the thickness, L_{pt}/w.

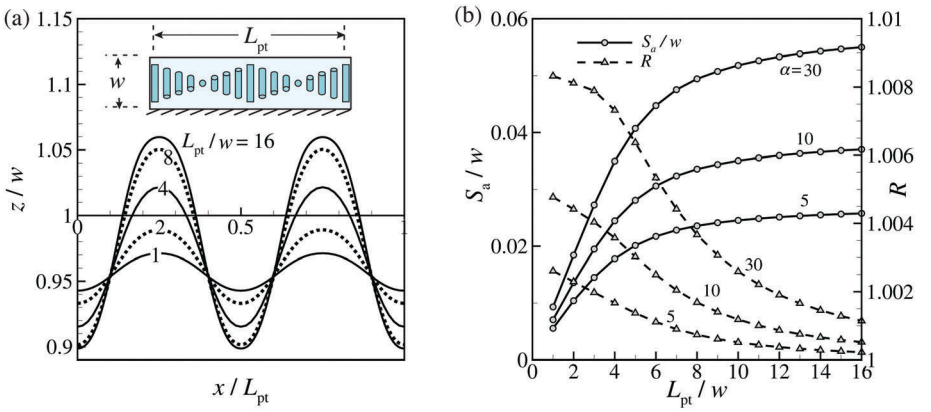

Fig. 10 (a) Normalized surface profiles for a full pitch of a regular fingerprint film with increasing L_{pt}/w. The inset shows a schematic of the film where the pitch helix is along the x-axis and all the director alignment is rotating inside the y–z plane. (b) Variations of the normalized average height S_a/w and the Wenzel roughness R against L_{pt}/w with α = 5, 10 and 30.

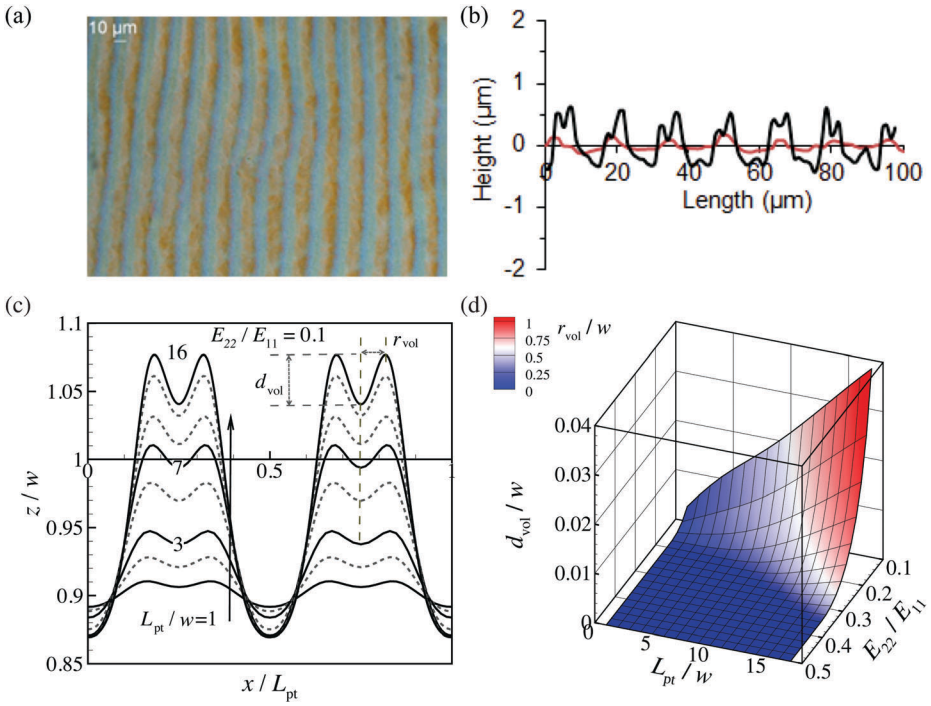

Fig. 11 (a) The polarization optical microscope image and (b) the measured surface profiles before (read line) and after illumination (black line) of a regular fingerprint film, in which volcano-shape tops were found. Reproduced with permission[27] (copyright 2014 Wiley). (c) Normalized surface profiles with various L_{pt}/w and a lower Young's moduli ratio E_{22}/E_{11} = 0.1. (d) Variations of the normalized volcano depth d_{vol}/w superimposed by a contour plot for the normalized volcano radius r_{vol}/w (d_{vol} and r_{vol} are defined in (c)) against the moduli ratio E_{22}/E_{11} and L_{pt}/w.

The evolution of the predicted surface undulations for various L_{pt}/w is shown in Fig. 10(b). The textures feature sinusoidal-like profiles and the surface change amplitude is enhanced for larger in-plane sizes. It is noteworthy to mention that, in contrast to the surface changes of the patterned films (*e.g.*, Fig. 5(e) and (f)) in which the textures converge to rectangular profiles as the in-plane dimensions increase, here the regular fingerprint films always retain a sinusoidal-like shape even for large L_{pt}/w. This is attributed to the continuous variation of the tilt angles of the directors along the planar pitch helices, which is every different from the alternating director alignment in the patterned films. Fig. 10(b) plots the normalized average height S_a/w and the Wenzel roughness R against L_{pt}/w for various α. The profile amplitude converges to similar values as experimentally-measured as L_{pt}/w increases.[27]

The measurements for a regular fingerprint film[27] (reproduced in Fig. 11(a) and (b)) show a well-controlled parallel pitch arrangement, while the measured surface profile shows noticeable volcano-like textures. We found this phenomenon to be correlated to the anisotropy in mechanical properties of the LC polymer. The predicted surface profiles using lower Young's moduli perpendicular to the director, $E_{22} = E_{33}$ = 100 MPa, relative to the 500 MPa for the default calculations of Table 1, are shown in Fig. 11(c). The volcanoes occur for all the tested geometries and the volcano sizes increase as L_{pt}/w increases. We define the volcano radius r_{vol} and the volcano depth d_{vol} (see Fig. 11(c)) to quantify the evolution of volcano-like textures, and study their dependencies on the mechanical properties and film dimensions. Fig. 11(d) shows the variations of the normalized volcano sizes, r_{vol}/w and d_{vol}/w, against the Young's moduli ratio E_{22}/E_{11} and L_{pt}/w. Volcanoes are about to be formed for any dimension if E_{22}/E_{11} is small enough (*e.g.*, 0.1), while for intermediate moduli ratios ($0.2 \leq E_{22}/E_{11} \leq 0.35$), volcanoes ensue only at large L_{pt}/w. The tendencies for the volcano radius and depth are generally the same: when a volcano has larger radius it is also more indented. This phenomenon opens the possibility to tailor the material properties and the geometries of fingerprint films in building controlled surface textures and hierarchical topographies.[80]

To model random fingerprint films, which is more common in the experimental implementation[27] (also see Fig. 2(c)), a nonuniform pitch configuration is introduced by setting non-parallel and curved helix pitches, mimicking the variability of the pitch alignment in real samples. Through the thickness the director is still assumed to be uniform due to the small film thickness. Fig. 12(a) shows the 3D topographical transformation of an exemplary random fingerprint film for three film sizes, $L_x = L_y = 4w$, $12w$ and $32w$, for which the surface textures show a close resemblance with the experimental measurements.[27] The corresponding surface profiles for a random y–z cross-section are plotted in Fig. 12(b), showing the effect of the film size (and thus the pitch length) on the amplitude of the surface profile. The corresponding roughness parameters are plotted in Fig. 12(c) against the normalized pitch length L_{pt}/w and the results from the regular fingerprint films are added for comparison. The horizontal error bars

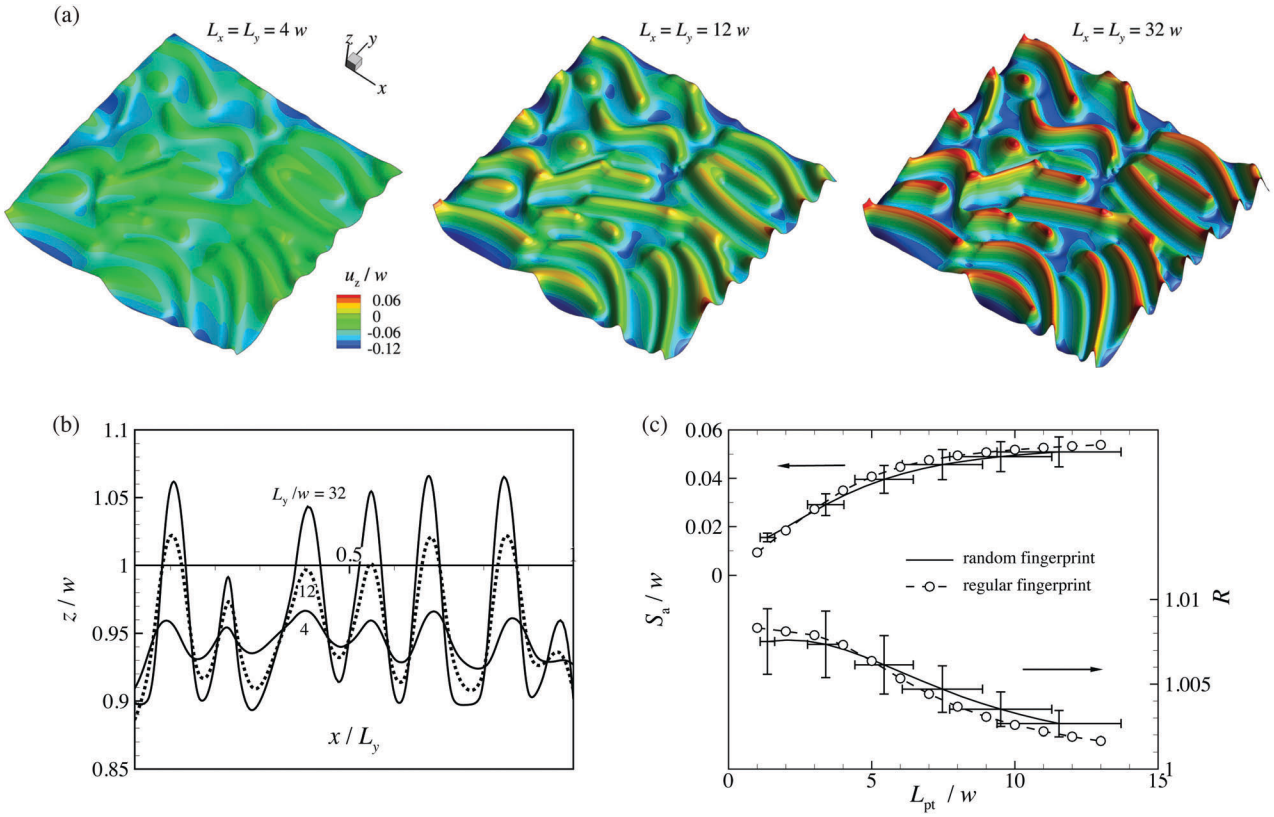

Fig. 12 (a) 3D topography images superimposed by contour plots for the normalized out-of-plane displacement for an irregular fingerprint film with a fixed thickness and increasing lateral dimensions, $L_x = L_y = iw$, $i = 4$, 12, and 32. (b) Evolution of the normalized surface profiles for various film dimensions. (c) Variations of the two roughness parameters of the random fingerprint films against L_{pt}/w. The horizontal and vertical error bars are the standard deviations of the ranges of the pitch lengths and the roughness, respectively.

indicate the standard deviations of the range of the pitch lengths and the vertical error bars are the standard deviations of the roughness parameters. The pitch length range and the roughness parameters are calculated by scanning multiple cross-sections of the topographies. The textures of the random fingerprints are three-dimensional in nature, in contrast to the regular fingerprints which are uniform along one of the in-plane directions (*y*-axis here), leading to a slightly higher Wenzel roughness for the random fingerprint films. On the other hand, the irregularity of the pitch arrangement brings in more constraints upon the out-of-plane displacements, leading to a slightly lower average height. However, the results of the regular fingerprints fall within the error bars of the random fingerprints, so that the differences, strictly speaking, are not statistically relevant.

4 Discussion and conclusion

We now compare the roughness parameter output, *i.e.*, S_a, R and the modulation (all defined in Section 3.4), for the three Azo-LC coatings studied here. The two types of ordered films are the linearly-patterned films and the regular fingerprint films. One of the merits of the fingerprint structure is its possibility of downsizing, with L_{pt}/w values in the range from 1 to 5 (ref. 27 and 75). These length scales are difficult to be reached using the linearly-patterned films with L/w values for the cholesteric/homeotropic films being larger than 50 (see ref. 24–26) and for the orthogonally-planar films larger than 10 (ref. 30). A roughness comparison is made here in terms of the geometric dimensionless numbers, *i.e.*, L/w and L_{pt}/w, in Fig. 13. A half pitch in the regular fingerprint coatings is equivalent to one unit cell for the patterned films. We assume that the cholesteric and homeotropic domains can be well-patterned at small scales. It is found that for a given in-plane length, L/w or $L_{pt}/2w$, the cholesteric/homeotropic film is able to yield the highest S_a, R and modulation compared to the other films. Relative to the cholesteric local illumination, the cholesteric and homeotropic domains can deform in opposite directions (up and down, respectively). The mechanical constraints predominately occur at the domain boundaries, while in the fingerprint films the continuous tilt angle rotation of the director leads to a higher suppression of the out-of-plane deformation due to mechanical constraints that are present throughout the film. However, when the design strategy is to maximize the modulation, the performance of the fingerprint film is close to the cholesteric/homeotropic film modulation (see Fig. 13(b)).

The roughness parameters of the irregular films, *i.e.*, the uniform and nonuniform polydomain films and random fingerprint films, are compared in Fig. 13(d). Like the fingerprint film,

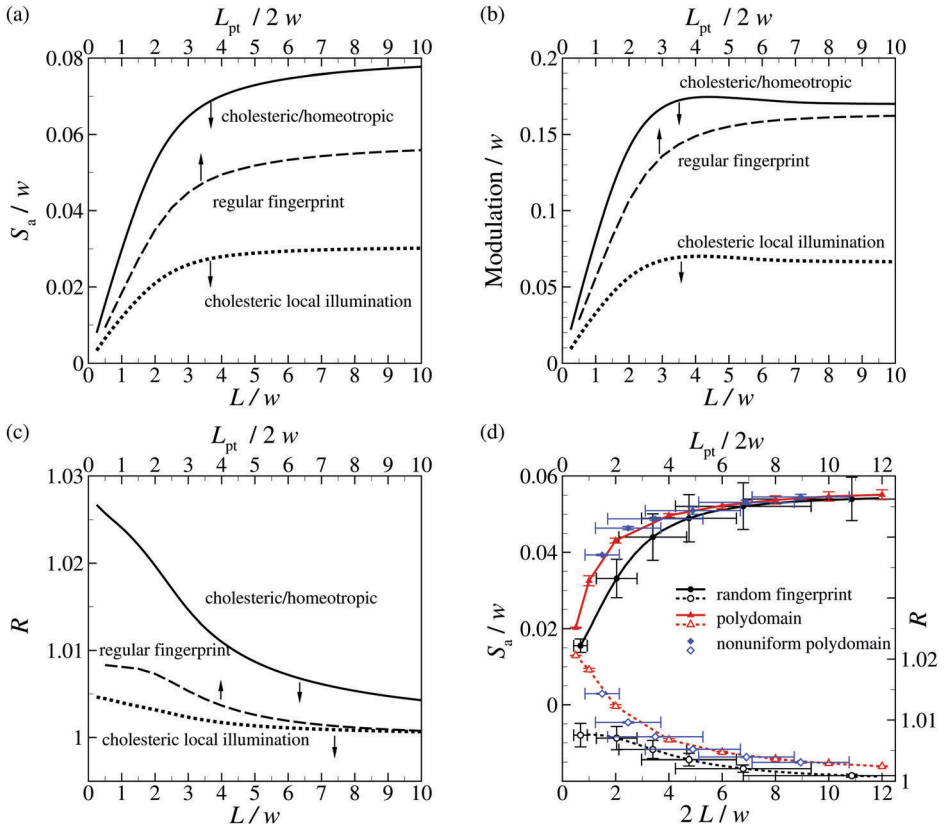

Fig. 13 Comparisons of the roughness parameters (a) S_a/w, (b) modulation/w and (c) Wenzel roughness R for the two linearly-patterned films and the regular fingerprint film. (d) Comparison of the S_a/w and R for the three random coatings, *i.e.*, the regular polydomain, nonuniform polydomain and irregular fingerprint films. The patterned films and the polydomain films use the bottom horizontal axis, while the regular and random fingerprint films use the top axis.

the polydomain films also feature small in-plane length scales, with aspect ratios in the range of 1 to 5 (ref. 29). The polydomain films can generate slightly larger values of the average height and Wenzel roughness than the random fingerprint films (Fig. 13(d)), but still lower than the cholesteric/homeotropic films in Fig. 13(a) and (c). The latter is due to the larger mechanical constraints in the irregular films due to the random distribution of the director and the domain sizes.

The comparisons above indicate that the regular fingerprint films are preferable for the design of miniaturized actuators where small wavelengths are required, but at the same time, also large corrugation modulations are requested. Linearly-patterned

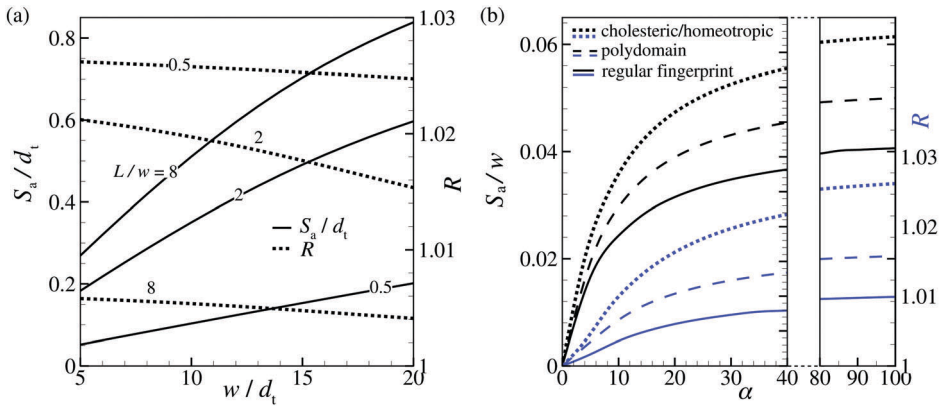

Fig. 14 (a) Variations of the average height normalized by the attenuation length of *trans* S_a/d_t and the Wenzel roughness R as functions of w/d_t with various L/w for the cholesteric/homeotropic film. (b) Comparison of S_a/w and R as functions of α with a fixed ratio α/β = 10 for three films. The in-plane dimensions of the three films are the same: L/w = 2 for the patterned films; L/w (aspect ratio) = 1 for the polydomain film; and L_{pt}/w = 4 for the regular fingerprint film.

cholesteric/homeotropic films, which are able to produce large undulations and rectangular corrugations at relative large feature sizes, might be desirable in applications like human haptic feedback technologies[35,81] and optical applications.[82] In addition, their regular textures and reproducible and well-structured design make them attractive for wettability switching[83] and friction manipulation.[28] Polydomain films, being able to output intermediate surface changes, feature ease in fabrication at controllable domain sizes.

Typical thicknesses of LC films are in the range of a few to tens of micrometers.[1,26,84] The attenuation length of *trans*, d_t, depends on the concentration of the azobenzene dye and the chemical composition of the Azo-LC polymer, and is considered a material constant here. In order to illustrate its influence for the cholesteric/homeotropic film, the thickness and in-plane length are increased simultaneously to keep the ratio L/w constant, and the variations of the average height (normalized by d_t) and the Wenzel roughness as a function of w/d_t are shown in Fig. 14(a). As w/d_t increases, the average height scales almost linearly with a slight non-linear reduction at large w/d_t due to a reduced *trans*-to-*cis* conversion level at large depths (see Fig. 3(a) and Fig. S1, ESI†). The Wenzel roughness remains almost unaffected, with a slight decrease due to the reduced conversion level at large depths.

The input light intensity is characterized by the dimensionless parameters α and β (see Section 2.2), which falls typically in the range of 100–1000 mW cm^{-2} (ref. 24, 25 and 29). The effect of the light intensity on the topographies is shown in Fig. 14(b), in which we compare the roughness parameters of three films with increasing α and a fixed ratio $\alpha/\beta = 10$. The S_a/w and R first increase with α and then they reach a plateau for all three films, corresponding to fully exhausted *trans*-to-*cis* conversion, in which the *cis* fraction gets saturated at $\alpha/(\alpha + \beta)$ for large α (see Fig. 3(b) and Fig. S2, ESI†). This prediction is in agreement with experiments,[24,27] in which the height variation converges under large intensity exposure.

In short, a computational model was developed to predict photo-switchable topographical changes for azobenzene-modified liquid crystal glassy polymer films. A non-linear light attenuation model was adopted to capture the director-dependent *trans*-to-*cis* isomerization, which was combined with an opto-mechanical constitutive relation to link the light-induced spontaneous deformation with the fraction of the *cis* azobenzenes. Distinct topographical textures were predicted for three types of Azo-LC films, *i.e.*, linearly-patterned, polydomain and fingerprint films, each of which features different director distributions, both ordered and disordered. The surface transformations depend on the film dimensions, opto-mechanical properties and illumination conditions. The topographical changes were quantified by roughness parameters related to height modulations and wetting properties. Close agreement was found between the predicted surface profiles and experimental results. Our computational simulations can serve as guide-lines to optimize topographical switching patterns and as a predictive tool to design new director distributions and surface undulations in functionalized devices and emerging applications such as light-controlled haptics, friction and wetting.

Conflicts of interest

There are no conflicts to declare.

Acknowledgements

This research forms a part of the research programme of the Dutch Polymer Institute (DPI), project #775 TOPSWITCH. The author would like to thanks Prof. Dirk J. Broer, Prof. Jaap den Toonder and Dr Danqing Liu for useful discussions.

References

1 T. J. White and D. J. Broer, *Nat. Mater.*, 2015, **14**, 1087–1098.
2 T. H. Ware, M. E. McConney, J. J. Wie, V. P. Tondiglia and T. J. White, *Science*, 2015, **347**, 982–984.
3 J. Lv, Y. Liu, J. Wei, E. Chen, L. Qin and Y. Yu, *Nature*, 2016, **537**, 179–184.
4 L. Hines, K. Petersen, G. Z. Lum and M. Sitti, *Adv. Mater.*, 2016, 1603483.
5 A. H. Gelebart, D. J. Mulder, M. Varga, A. Konya, G. Vantomme, E. Meijer, R. L. Selinger and D. J. Broer, *Nature*, 2017, **546**, 632–636.
6 T. Ube, K. Minagawa and T. Ikeda, *Soft Matter*, 2017, **13**, 5820–5823.
7 T. Ikeda, J. Mamiya and Y. Yu, *Angew. Chem., Int. Ed.*, 2007, **46**, 506–528.
8 H. Yu and T. Ikeda, *Adv. Mater.*, 2011, **23**, 2149–2180.
9 S. Chatani, C. J. Kloxin and C. N. Bowman, *Polym. Chem.*, 2014, **5**, 2187–2201.
10 H. K. Bisoyi and Q. Li, *Chem. Rev.*, 2016, 2994–3010.
11 Y. Yu, M. Nakano and T. Ikeda, *Nature*, 2003, **425**, 145.
12 C. L. van Oosten, D. Corbett, D. Davies, M. Warner, C. W. Bastiaansen and D. J. Broer, *Macromolecules*, 2008, **41**, 8592–8596.
13 T. J. White, N. V. Tabiryan, S. V. Serak, U. A. Hrozhyk, V. P. Tondiglia, H. Koerner, R. A. Vaia and T. J. Bunning, *Soft Matter*, 2008, **4**, 1796–1798.
14 K. D. Harris, R. Cuypers, P. Scheibe, C. L. van Oosten, C. W. M. Bastiaansen, J. Lub and D. J. Broer, *J. Mater. Chem.*, 2005, **15**, 5043–5048.
15 C. L. van Oosten, K. Harris, C. Bastiaansen and D. Broer, *Eur. Phys. J. E: Soft Matter Biol. Phys.*, 2007, **23**, 329–336.
16 M. Warner, C. Modes and D. Corbett, *Proc. R. Soc. A*, 2010, **466**, 2975–2989.
17 O. M. Wani, H. Zeng and A. Priimagi, *Nat. Commun.*, 2017, **8**, 15546.
18 M. Camacho-Lopez, H. Finkelmann, P. Palffy-Muhoray and M. Shelley, *Nat. Mater.*, 2004, **3**, 307–310.
19 S. Palagi, A. G. Mark, S. Y. Reigh, K. Melde, T. Qiu, H. Zeng, C. Parmeggiani, D. Martella, A. Sanchez-Castillo and N. Kapernaum, *et al.*, *Nat. Mater.*, 2016, **15**, 647–653.
20 M. Yamada, M. Kondo, R. Miyasato, Y. Naka, J.-i. Mamiya, M. Kinoshita, A. Shishido, Y. Yu, C. J. Barrett and T. Ikeda, *J. Mater. Chem.*, 2008, **19**, 60–62.

21 M. Yamada, M. Kondo, J.-i. Mamiya, Y. Yu, M. Kinoshita, C. J. Barrett and T. Ikeda, *Angew. Chem., Int. Ed.*, 2008, **47**, 4986–4988.
22 C. L. van Oosten, C. W. Bastiaansen and D. J. Broer, *Nat. Mater.*, 2009, **8**, 677–682.
23 A. H. Gelebart, M. Mc Bride, A. P. H. J. Schenning, C. N. Bowman and D. J. Broer, *Adv. Funct. Mater.*, 2016, **26**, 5322–5327.
24 D. Liu, C. W. M. Bastiaansen, J. M. J. den Toonder and D. J. Broer, *Macromolecules*, 2012, **45**, 8005–8012.
25 D. Liu, C. W. M. Bastiaansen, J. M. J. den Toonder and D. J. Broer, *Angew. Chem., Int. Ed.*, 2012, **51**, 892–896.
26 D. Liu and D. J. Broer, *Liq. Cryst. Rev.*, 2013, **1**, 20–28.
27 D. Liu and D. J. Broer, *Angew. Chem., Int. Ed.*, 2014, **126**, 4630–4634.
28 D. Liu and D. J. Broer, *Soft Matter*, 2014, **10**, 7952–7958.
29 D. Liu, L. Liu, P. R. Onck and D. J. Broer, *Proc. Natl. Acad. Sci. U. S. A.*, 2015, **112**, 3880–3885.
30 M. Hendrikx, A. P. H. J. Schenning and D. J. Broer, *Soft Matter*, 2017, **13**, 4321–4327.
31 N. Wagner and P. Theato, *Polymer*, 2014, **55**, 3436–3453.
32 P. K. Roy, R. Pant, A. K. Nagarajan and K. Khare, *Langmuir*, 2016, 5738–5743.
33 O. Guselnikova, J. Svanda, P. Postnikov, Y. Kalachyova, V. Svorcik and O. Lyutakov, *Adv. Mater. Interfaces*, 2016, 1600886.
34 Y. Huang, B. B. Stogin, N. Sun, J. Wang, S. Yang and T.-S. Wong, *Adv. Mater.*, 2016, 1604641.
35 N. Torras, K. Zinoviev, C. Camargo, E. M. Campo, H. Campanella, J. Esteve, J. Marshall, E. Terentjev, M. Omastová and I. Krupa, *et al.*, *Sens. Actuators, A*, 2014, **208**, 104–112.
36 C. J. Camargo, H. Campanella, J. E. Marshall, N. Torras, K. Zinoviev, E. M. Terentjev and J. Esteve, *Macromol. Rapid Commun.*, 2011, **32**, 1953–1959.
37 C. Camargo, H. Campanella, J. Marshall, N. Torras, K. Zinoviev, E. Terentjev and J. Esteve, *J. Micromech. Microeng.*, 2012, **22**, 075009.
38 H. N. Kim, K.-J. Jang, J.-Y. Shin, D. Kang, S. M. Kim, I. Koh, Y. Hong, S. Jang, M. S. Kim and B.-S. Kim, *et al.*, *ACS Nano*, 2017, 730–741.
39 M. A. C. Stuart, W. T. Huck, J. Genzer, M. Müller, C. Ober, M. Stamm, G. B. Sukhorukov, I. Szleifer, V. V. Tsukruk and M. Urban, *et al.*, *Nat. Mater.*, 2010, **9**, 101–113.
40 D. Corbett and M. Warner, *Phys. Rev. Lett.*, 2006, **96**, 237802.
41 D. Corbett and M. Warner, *Phys. Rev. Lett.*, 2007, **99**, 174302.
42 M. L. Smith, K. M. Lee, T. J. White and R. A. Vaia, *Soft Matter*, 2014, **10**, 1400–1410.
43 L. Cheng, Y. Torres, K. Min Lee, A. J. McClung, J. Baur, T. J. White and W. S. Oates, *J. Appl. Phys.*, 2012, **112**, 013513.
44 K. Fuchi, T. H. Ware, P. R. Buskohl, G. W. Reich, R. A. Vaia, T. J. White and J. J. Joo, *Soft Matter*, 2015, **11**, 7288–7295.
45 M. Knežević, M. Warner, M. Čopič and A. Sánchez-Ferrer, *Phys. Rev. E: Stat., Nonlinear, Soft Matter Phys.*, 2013, **87**, 062503.
46 J. Choi, H. Chung, J.-H. Yun and M. Cho, *Appl. Phys. Lett.*, 2014, **105**, 221906.
47 P. M. Hogan, A. R. Tajbakhsh and E. M. Terentjev, *Phys. Rev. E: Stat., Nonlinear, Soft Matter Phys.*, 2002, **65**, 041720.
48 M. Kondo, M. Sugimoto, M. Yamada, Y. Naka, J.-i. Mamiya, M. Kinoshita, A. Shishido, Y. Yu and T. Ikeda, *J. Mater. Chem.*, 2010, **20**, 117–122.
49 Y. Yu, M. Nakano, A. Shishido, T. Shiono and T. Ikeda, *Chem. Mater.*, 2004, **16**, 1637–1643.
50 L. B. Braun, T. G. Linder, T. Hessberger and R. Zentel, *Polymers*, 2016, **8**, 435.
51 B. Zhu, M. Barnes, H. Kim, M. Yuan, H. Ardebili and R. Verduzco, *Sens. Actuators, B*, 2017, **244**, 433–440.
52 H. Finkelmann, E. Nishikawa, G. Pereira and M. Warner, *Phys. Rev. Lett.*, 2001, **87**, 015501.
53 K. Kumar, A. P. Schenning, D. J. Broer and D. Liu, *Soft Matter*, 2016, **12**, 3196–3201.
54 Y. Zhao and T. Ikeda, *Smart light-responsive materials: azobenzene-containing polymers and liquid crystals*, John Wiley & Sons, 2009.
55 D. Corbett and M. Warner, *Phys. Rev. E: Stat., Nonlinear, Soft Matter Phys.*, 2008, **78**, 061701.
56 M. Warner and L. Mahadevan, *Phys. Rev. Lett.*, 2004, **92**, 134302.
57 D. Corbett and M. Warner, *Phys. Rev. E: Stat., Nonlinear, Soft Matter Phys.*, 2008, **77**, 051710.
58 D. Statman and I. Janossy, *J. Chem. Phys.*, 2003, **118**, 3222.
59 Hibbitt, Karlsson and Sorensen, *ABAQUS/standard: User's Manual*, Hibbitt, Karlsson & Sorensen, 1998, vol. 1.
60 I. Heynderickx, D. Broer, H. Van Den Boom and W. Teesselink, *J. Polym. Sci., Part B: Polym. Phys.*, 1992, **30**, 215–220.
61 M. Warner and E. M. Terentjev, *Liquid crystal elastomers*, Oxford University Press, 2003, vol. 120.
62 G. N. Mol, K. D. Harris, C. W. Bastiaansen and D. J. Broer, *Adv. Funct. Mater.*, 2005, **15**, 1155–1159.
63 Q. Liu, Y. Zhan, J. Wei, W. Ji, W. Hu and Y. Yu, *Soft Matter*, 2017, **13**, 6145–6151.
64 L. Liu and P. R. Onck, in *Chapter of Responsive Polymer Surfaces – Dynamics in Surface Topographies and Properties*, ed. D. Liu and D. J. Broer, Wiley, 2017.
65 H. Zeng, D. Martella, P. Wasylczyk, G. Cerretti, J.-C. G. Lavocat, C.-H. Ho, C. Parmeggiani and D. S. Wiersma, *Adv. Mater.*, 2014, **26**, 2319–2322.
66 H. Zeng, P. Wasylczyk, G. Cerretti, D. Martella, C. Parmeggiani and D. S. Wiersma, *Appl. Phys. Lett.*, 2015, **106**, 111902.
67 K. Nickmans, G. M. Bögels, C. Sánchez-Somolinos, J. N. Murphy, P. Leclère, I. K. Voets and A. P. Schenning, *Small*, 2017, **13**, 1701043.
68 E. Gadelmawla, M. Koura, T. Maksoud, I. Elewa and H. Soliman, *J. Mater. Process. Technol.*, 2002, **123**, 133–145.
69 I. P. Arbizu and C. L. Perez, *J. Mater. Process. Technol.*, 2003, **143**, 390–396.
70 R. J. Crawford, H. K. Webb, V. K. Truong, J. Hasan and E. P. Ivanova, *Adv. Colloid Interface Sci.*, 2012, **179**, 142–149.
71 M. Sedlaček, B. Podgornik and J. Vižintin, *Tribol. Int.*, 2012, **48**, 102–112.

72 R. N. Wenzel, *Ind. Eng. Chem. Res.*, 1936, **28**, 988–994.
73 A. Goulet-Hanssens, T. C. Corkery, A. Priimagi and C. J. Barrett, *J. Mater. Chem. C*, 2014, **2**, 7505–7512.
74 R. Eelkema, M. M. Pollard, J. Vicario, N. Katsonis, B. S. Ramon, C. W. Bastiaansen, D. J. Broer and B. L. Feringa, *Nature*, 2006, **440**, 163.
75 H. Nagai, X. Liang, Y. Nishikawa, K. Nakajima and K. Urayama, *Macromolecules*, 2016, 9561–9567.
76 R. S. Kularatne, H. Kim, M. Ammanamanchi, H. N. Hayenga and T. H. Ware, *Chem. Mater.*, 2016, **28**, 8489–8492.
77 Z.-g. Zheng, Y. Li, H. K. Bisoyi, L. Wang, T. J. Bunning and Q. Li, *Nature*, 2016, **531**, 352–356.
78 Z.-g. Zheng, R. S. Zola, H. K. Bisoyi, L. Wang, Y. Li, T. J. Bunning and Q. Li, *Adv. Mater.*, 2017, 1701903.
79 R. Eelkema, M. M. Pollard, N. Katsonis, J. Vicario, D. J. Broer and B. L. Feringa, *J. Am. Chem. Soc.*, 2006, **128**, 14397–14407.
80 M. K. McBride, M. Hendrikx, D. Liu, B. T. Worrell, D. J. Broer and C. N. Bowman, *Adv. Mater.*, 2017, **29**, 1606509.
81 C. Mavroidis, C. Pfeiffer, J. Celestino and Y. Bar-Cohen, SPIE's 7th Annual International Symposium on Smart Structures and Materials, 2000, pp. 300–310.
82 C. Zhang, J. Fang, W. Yang, Q. Song and S. Xiao, *Adv. Opt. Mater.*, 2017, **5**, 1700469.
83 T. Verho, J. T. Korhonen, L. Sainiemi, V. Jokinen, C. Bower, K. Franze, S. Franssila, P. Andrew, O. Ikkala and R. H. Ras, *Proc. Natl. Acad. Sci. U. S. A.*, 2012, **109**, 10210–10213.
84 L. T. de Haan, A. P. Schenning and D. J. Broer, *Polymer*, 2014, **55**, 5885–5896.

